False Alarm Reduction of Ground Penetrating Radar Returns through Multisensor Fusion

Yönet Eracar, Charles DiMarzio and Mieczyslaw M. Kokar

Northeastern University
Boston, Massachusetts 02115

Abstract

In this work, we present a methodology for fusing high frequency and low frequency radar images. The goal of this system is to find the strong surface clutter which is common to high and low frequency radar images and to subtract (de-fuse) this common component from the low frequency image to extract subsurface information.

1 Introduction

One of the most severe limitations of GPR detection of buried targets is the masking of these weak target returns by a strong surface clutter element. In this research effort we investigated methods for fusing high frequency radar data (strong clutter component, low penetration) and low frequency radar data (deeper subsurface penetration, but also strong clutter component) in order to reduce the effect of clutter. Since the clutter component is common to both sets of radar data, we focussed our efforts on subtracting this common component from the low frequency image to obtain the subsurface image.

In the approach presented in this report we first apply image enhancement algorithms to both the high and low frequency images, then we detect features in both images (like roads, bushes, main washes), align the features, and finally subtract the features that are common to both images. The idea is to achieve the same effect as in pixel-to-pixel fusion, yet avoid the difficulties with both high computational complexity and the lack of physical characteristics that would allow recognition and association of pixels representing the same scattering point in the penetrated soil.

2 Description of Experimental Data

In our experiments we used data from the 1993 ground penetration experiment in Yuma, AZ [8]. Specifically, we utilized data from two sensors: a Stanford Research International (SRI) impulse synthetic aperture radar (SAR) operating between 100 and 500 Mhz and the MIT Lincoln Laboratory ground-based wide-band SAR, capable of operating from 150 MHz to above 10 GHz. In the rest of this report we will refer to these two radars as SRI and LLMMW.

The SRI data covers a rectangular area of 0.89 by 2.1 kilometers. Both the range and cross range pixel spacings are 0.6 meters. The LLMMW data is a combination of six data files, each covering an area of 0.47 by 0.47 kilometers. For each image, both the cross range and range pixel spacings are 0.2287 meters. These six images combine to produce one large image which covers roughly the same area of the Yuma desert as does the single SRI image.

In the Yuma experiment, a number of targets were deployed and buried. The area we are dealing with includes the wire deployment, some washes, and a road that runs parallel to the flight path. Most of the image is desert clutter. The SRI data (the clutter backscatter, σ_0) has a range of $-72dB$ to $25dB$ and a mean at $-28dB$.

Both sets of data were stored as floating point (four bytes) using a total of 84MB of memory space. Therefore, we extracted a small portion of the data which contains a section of the wire deployment along with some other features like the main washes (see Figure 1). A small data file speeds up the experiments and the process of testing of our algorithms.

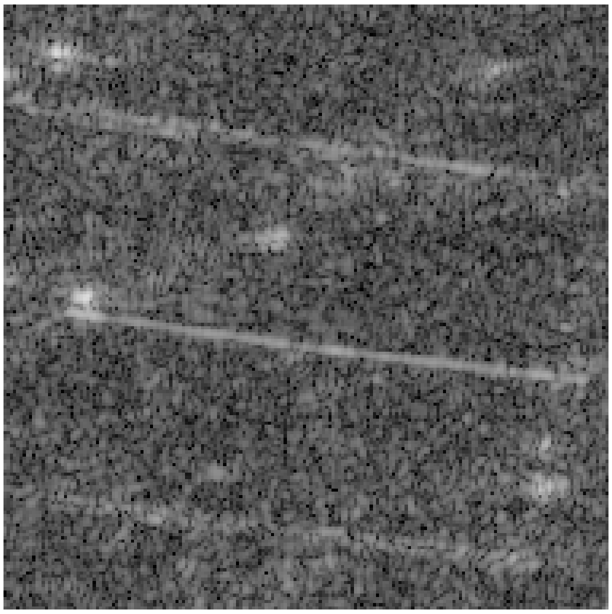

Figure 1: **SRI image containing the wire deployment**

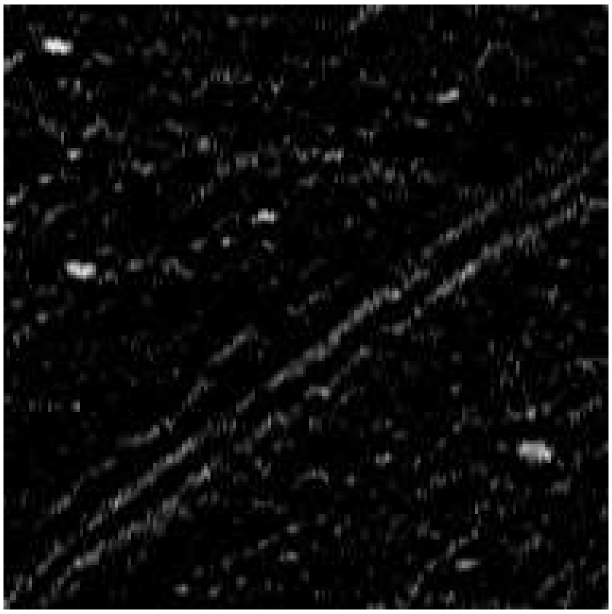

Figure 2: **LLMMW image covering the same area with wire deployment**

3 Technical Approach

As a result of numerous experiments with processing the ground penetration radar images, we proposed a procedure that includes the following five steps (see Figure 3): *Image Enhancement, Feature Detection, Association, Subtraction*, and *Detection*. The algorithms for the first four steps are described in the following three subsections. Detection is described in Section 4.

3.1 Image Enhancement

Since the data contain noise and cover a wide range of dB values, we had to choose a working range for both images, which would give us a better contrast of visualization. First, we analyzed slices from the two images in order to determine the variation of the σ_0 (surface backscatter) val-

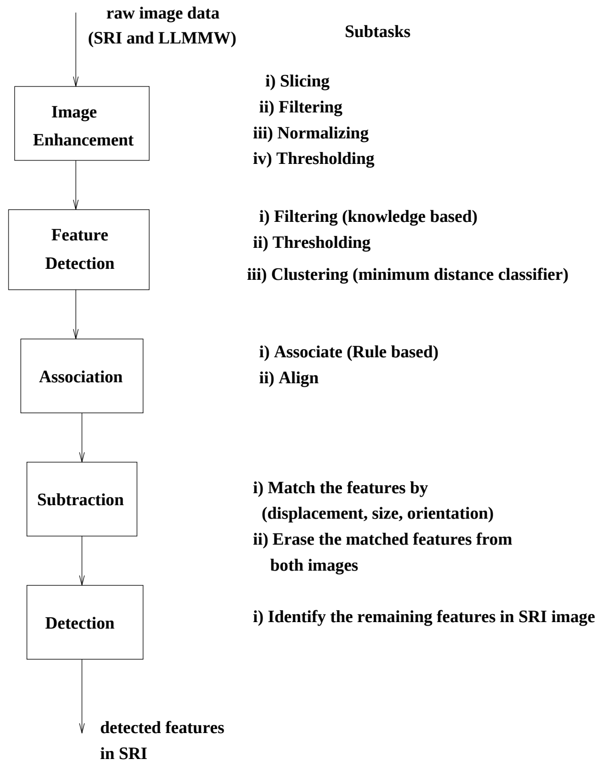

Figure 3: **Processing Diagram**

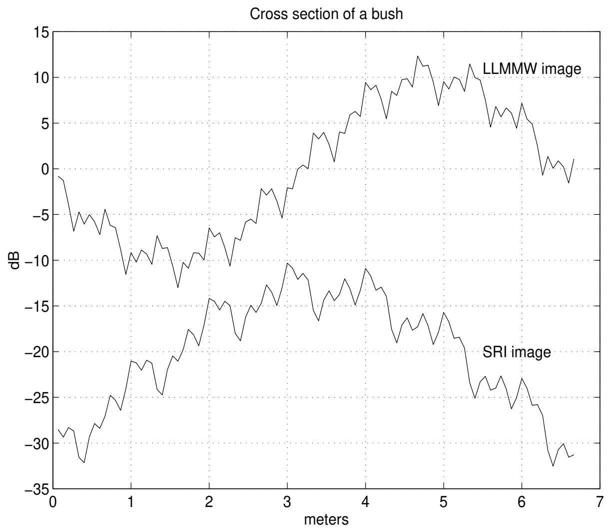

Figure 4: **Comparison of the same bush seen in SRI and LLMMW**

ues around certain features, like road and bush. The goal was to identify a common pattern (in terms of dB values) associated with bushes. This pattern is necessary for identifying this feature and for selecting threshold values. As can be seen in Figure 4, for all bushes in the LLMMW image the pattern has a sinusoidal shape: a bright side (perpendicular to the direction of coming radar signal) and a dark side (shadow). However, in the SRI image, the shadow effect is less visible and a bell-like curve is dominant. We used these two curves as one dimensional convolution masks to filter out spikes and to emphasize the peaks of these features.

To reduce the blurring of edges, we applied the Median Filter [11]. In order to avoid loosing important details, like the road, we had to choose the best size of the filter. We experimentally selected a Median Filter with a window of 5 by 5 pixels. Once the images are filtered, histograms of gray-levels are constructed and the upper and lower limits of the dB values (I_{low}, I_{up}) are determined according to the information we obtained from the slicing procedure. I_{low} is the smaller of the lower limits obtained from the histogram and from the slicing procedure. I_{up} is the larger of the upper limits. Then, the images are normalized according to the following rule:

$$I_N(x,y) = \begin{cases} 0 & \text{if } I_0(x,y) \geq I_{up} \\ 0 & \text{if } I_0(x,y) \leq I_{low} \\ \frac{I_O(x,y)-I_{low}}{I_{up}-I_{low}} 255 & \text{otherwise} \end{cases}$$

where I_0 represents the original image and I_N represents the normalized image.

In order to unify the resolution of the two images, the following Non-Integer Scaling function is applied to the LLMMW image:

$$I_{scaled}(x', y') = \frac{\sum_{i,j} w_{i,j} I(x,y)}{\alpha^2}$$

where

$$\alpha = \frac{SRI\_pixel\_spacing}{LLMMW\_pixel\_spacing}$$

and w_{ij} is the weight of the pixel $I(x,y)$. The weight is 1 if the whole pixel is contained within the window in the higher resolution image corresponding to the one pixel in the lower resolution window. Otherwise, the weight is the fraction of the pixel area contained in the window. The summation is over all the pixels of the window. Figure

1 and Figure 2 show two images that have been normalized, scaled and aligned. The alignment in this case was done manually based on reference points.

3.2 Feature Detection

As we have shown in our previous report [3], edge detection (Sobel, Laplacian Operators) and segmentation methods that are typically used in computer vision [7, 4], do not provide satisfactory performance on SAR images, primarily because in SAR images the underlying assumption of continuity in the change of intensity does not apply. Since common edge detection methods have failed, tools like Hough Transform couldn't be utilized [2]. For this reason, a *statistical classifier* was implemented and used for feature detection. In our case, features were bushes, washes and road in both images, and additionally, wires in the SRI image. The classifier groups pixels into classes corresponding to particular features. These features are thus represented by *class identifiers*.

In our experiments we used a variation of the *MacQueen k-means* classification method [6]. Since the MacQueen k-means method needs the number of classes as input (which we did not have), we modified the method so that it determines the number of classes dynamically.

In our algorithm, the classification rule consists of three parts. The algorithm first selects pixels (*exemplars*) to represent initial classes and determines the number of these initial classes by using the following procedure. The algorithm selects the maximum intensity pixel as an exemplar and surrounds it with a circle of the radius equal to the radius of a bush. This radius is presumed to be known. Then the algorithm selects another exemplar (maximum intensity pixel) from the pixels outside of the circle. This procedure is iterated until all the pixels are inside of at least one circle. The result is a list of initial exemplars and the initial number of classes k.

In the next step, the classification algorithm assigns each pixel (except for those selected as exemplars) to one of the classes using the classification decision rules $d_i(p) = w_r$ shown below:

$$d_1(p) = w_r \iff \|v_r - p\| = \min_{s=1,\dots,k} \|v_s - p\| \quad (1)$$

$$d_2(p) = w_r \iff \|v_r - p\| \leq max\_distance. \quad (2)$$

$$d_3(p) = w_r \iff I(p) \geq min\_intensity. \quad (3)$$

where p represents a pixel, w_r represents the $r-th$ class, $\|v_r - p\|$ represents the Euclidian distance between the center v_r of the class w_r and the pixel p. These rules require two thresholding parameters: $max\_distance$, which limits the size of one class, and $min\_intensity$, which filters out the pixels with low intensity.

After a new pixel p is added to the class i the centroid v_i for this class is updated according to the following rule:

$$v_i = \frac{1}{k_i + 1}(k_i v_i + p) \quad (4)$$

$$k_i = k_i + 1 \quad (5)$$

where k_i is the number of pixels included in class i, v_i is the center of the class and p is the newly added pixel. These centroids are used as new exemplars in the next pass. The process is iterated until no re-assignments of pixels to classes are made in one pass.

Additionally, for each class the algorithm computes the number of pixels (*population*), shape moments $\sigma_x, \sigma_y, \sigma_{xy}$, and orientation θ which is valid for the elongated regions (wires, road). Orientation is defined as the direction of the longer side of a minimum bounding rectangle and calculated as

$$\theta = \frac{1}{2} \arctan \frac{b}{a-c} \quad (6)$$

where

$$a = \sum_i \sum_j (j - x_{center})^2 p_{i,j} \quad (7)$$

$$b = 2 \sum_i \sum_j ((i - y_{center})(j - x_{center})) p_{i,j} \quad (8)$$

$$c = \sum_i \sum_j ((i - y_{center}))^2 p_{i,j} \quad (9)$$

Classes for which $population < min\_population$ are discarded.

3.3 Association & Subtraction

After features are extracted in both SRI and LLMMW images, the features are input to the association algorithm. The features in the SRI (lower frequency) image that are associated with at least one feature in the LLMMW image are subtracted from the low frequency image. The association algorithm is based on the following cost function $C(i, j)$ calculated for all pairs of features w_i, w_j in the two images:

$$
\begin{aligned}
C(i,j) &= c_{disp} + c_{pop} + c_{orient} && (10)\\
c_{disp} &= w_{disp} \cdot \|v_i - v_j\| && (11)\\
c_{pop} &= w_{pop} \cdot (pop(i) - pop(j)) && (12)\\
c_{orient} &= w_{orient} \cdot (\theta_i - \theta_j), && (13)
\end{aligned}
$$

where w_{disp}, w_{pop} and w_{orient} are the weights for the three cost components: *displacement*, *population* and *orientation*. These weights were determined experimentally in order to maximize correct association. A pair of features (w_i, w_j) is associated if the value of the cost function $C(i, j)$ is less than some threshold. Methods for defining various cost functions and for determining weights are described, for instance, in [10], [1].

The algorithm operates in the feature space; the complexity of the algorithm is at the order of $O(N_{SRI} \cdot N_{LLMMW})$, where N_{SRI} is the number of features detected in the SRI image and $N_{LLMMW})$ is the number of features detected in the LLMMW image. The resultant detection image after the subtraction is shown in Figure 5.

Figure 5: **The resultant image after subtraction**

4 Results

The focus of this research is to develop algorithms for detection of wires. Other features, like roads and bushes, were extracted for two reasons: feature-to-feature association and then subtraction. The features like roads and bushes constitute the clutter in the ground penetrating scenario. They show up in both the high frequency and the low frequency radar signals. Therefore they can be subtracted. Underground targets, like wires, on the other hand, cannot be detected by a high frequency radar. The main idea of our approach is that these features will not be associated with any other features in the high frequency radar, and therefore will remain in the low frequency image after subtraction.

To evaluate the validity of this idea we analyzed the remaining features in the low frequency image after subtraction of common features. These features were considered as *detections* of wires. The criteria used for this evaluation was the probability of detection (PD) and the probability of false alarm (PFA).

In our experiments we did not have the ground truth information and, therefore, we had to use some estimates of these two parameters. To assess the probability of detection we counted those clusters in the resulting image that covered segments of wires. Probability of detection was calculated as the ratio of the area of detected segments of wires to the whole area of wires.

To assess the probability of false alarms, we first applied the clustering algorithm to the raw low frequency image and counted the number of detected clusters. Among those, we counted the number of clusters that were not part of the wires. The ratio of the latter and the former numbers gave us the probability of false alarm. The same baseline, i.e., the same number of detections, was used to calculate the probability of false alarms after subtraction. We call it *relative probability of false alarms* since it uses only the number of clusters detected in the raw image, rather than the number of all possible clusters in the image (which would be much higher).

As described earlier, our algorithm uses a number of parameters that need to be selected or tuned. Fine-tuning of these parameters is essential to the success of the algorithm. Especially, three of the parameters, *min_intensity*, *min_population* and *max_displacement* were found to be critical for obtaining higher probability of detection for a given probability of false alarm.

In order to test the sensitivity of the algorithm to the three parameters, we calculated the probability of detection for various probabilities of false alarms. The probability of false alarm was varied by varying the *min_intensity* threshold. We developed two sets of ROC curves: one for a fixed *min_population* and one for a fixed *max_displacement*. These curves are shown in Figure 6. The top figure shows two ROC curves for the *max_displacement* fixed at a level that guarantees the maximum PD value. The bottom figure shows the ROC curves for two different *min_population* values, while *max_displacement* is fixed. The bottom (continuous) line in both figures represents the ROC curve for detection in the single (SRI) image.

5 Conclusions and Future Research

The main goal of this research was to investigate the idea of subtracting the high frequency SAR image from the low frequency SAR image in order to eliminate the impact of surface clutter on the detection of buried objects. The focus of our investigation was on detecting buried wires. We proposed a method in which two images are first preprocessed for image enhancement. Then features are detected in both images and feature-to-feature association is performed. Finally, features that have their counterparts through the association process are removed (subtracted) from the low frequency image. The remaining features represent buried targets (in our case, wires).

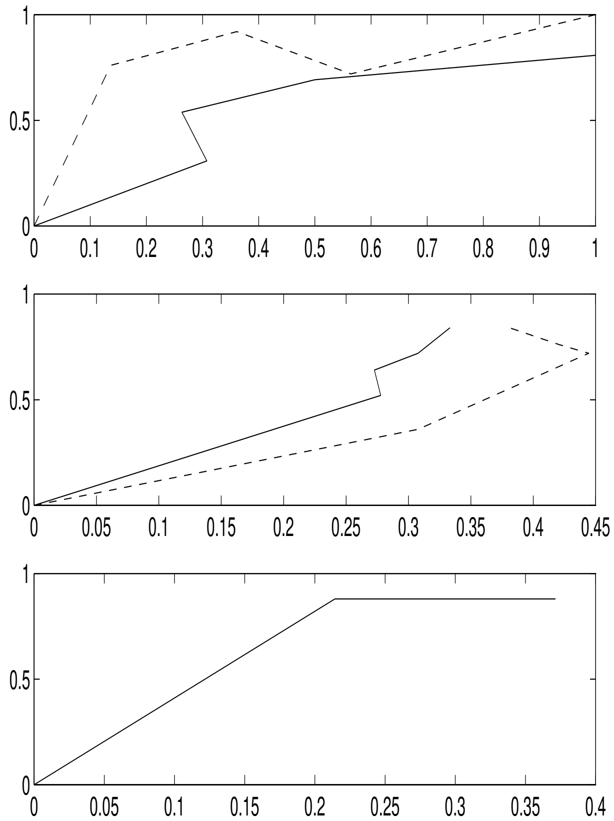

Figure 6: **ROC curves for different** *min_population* **values (top) and for different** *max_displacement* **values (bottom)**

As can be seen from the results shown in Figure 6, the algorithm proposed in this paper significantly improves target detection in terms of probability of detection and probability of false alarms. It is, however, important to understand that these results were obtained after experimenting with various image processing algorithms, various sequences of processing, and various parameters that had to be tuned. Also, the algorithm was evaluated only on a limited set of data. Different data might require re-tuning of the parameters to obtain comparable detection results. Figure 6 shows the sensitivity of the algorithm to these parameters.

Overall, these results are a positive step towards a fully automatic algorithm for detection of specific underground targets. Adaptive algorithms are known in the literature and can be investigated for the applicability to the ground penetrating radar scenarios. Also, phenomenology of underground SAR imaging has been investigated (cf.[9]) and documented. This phenomenology constitutes the base for the selection of image processing algorithms and their parameters. It can be implemented using the combination of symbolic and quantitative processing (cf. [5].

Acknowledgments

This research was supported by a grant from the Army Research Laboratory directed by Jeff Sichina and Karl Kappra. The data from the 1993 Yuma Experiment were obtained from MIT Lincoln Laboratory; we thank E.M.Adams for help. The authors wish to thank Serpil Ayasli and Jen King Jao for valuable suggestions related to this research task.

References

[1] D. H. Ballard and C. M. Brown. *Computer Vision.* Prentice-Hall, Englewood Cliffs, NJ, 1982.

[2] R. O. Duda and P. E. Hart. Using the hough transforms to detect lines and curves in pictures. *Communications of the ACM*, 15, no. 1:11–15, 1972.

[3] Y. Eracar, C. DiMarzio, and M. M. Kokar. Technical Report Research Progress Reports, Center for Electromagnetics Research, Northeastern University, Boston, 1995.

[4] W. E. L. Grimson. *From Images to Surfaces: A Computational Study of the Human Early Visual System.* MIT Press, Cambridge, MA, 1981.

[5] M. M. Kokar. On consistent symbolic representations of general dynamic systems. *IEEE Transactions on Systems, Man and Cybernetics*, 25, no. 8:1231–1242, 1995.

[6] J. MacQueen. Some methods for classification and analysis of multivariate observations. In *Proceedings of the 5th Berkeley Symposium-1*, pages 281–297, 1967.

[7] D. Marr. *A Computational Investigation into the Human Representation and Processing of Visual Information.* W. H. Freeman and Co., San Francisco, 1982.

[8] M. I. Mirkin, T. O. Grosch, T. J. Murphy, and S. Ayasli. Results of june 1993 yuma ground penetration experiment. In *Aerial Surveillance Sensing Including Obscured and Underground Object Detection*, pages 4–15. SPIE-The International Society for Optical Engineering, 1994.

[9] M. I. Mirkin, C. F. Lee, T. O. Grosch, B. E. Hodges, and S. Ayasli. Results on ground penetration sar phenomenology from june 1993 yuma experiment. pages –, 1994.

[10] A. Rosenfeld and A. C. Kak. *Digital Signal Processing.* Academic Press, New York, 1982.

[11] S. G. Tyan. *Median Filtering, Deterministic Properties*, volume 2. 1981.